Detectable Anthropogenic Shift toward Heavy Precipitation over Eastern China

Shuangmei Ma,[a,b] Tianjun Zhou,[b,c] Dáithí A. Stone,[d] Debbie Polson,[e]
Aiguo Dai,[f] Peter A. Stott,[g] Hans von Storch,[h] Yun Qian,[i] Claire Burke,[g]
Peili Wu,[g] Liwei Zou,[a] and Andrew Ciavarella[g]

[a] Institute of Climate System, Chinese Academy of Meteorological Sciences, Beijing, China
[b] LASG, Institute of Atmospheric Physics, Chinese Academy of Sciences, Beijing, China
[c] Joint Center for Global Change Studies, Beijing, China
[d] Lawrence Berkeley National Laboratory, Berkeley, California
[e] School of GeoSciences, Grant Institute, University of Edinburgh, Edinburgh, United Kingdom
[f] Department of Atmospheric and Environmental Sciences, University at Albany, State University of New York, Albany, New York
[g] Met Office Hadley Centre, Exeter, United Kingdom
[h] KlimaCampus, University of Hamburg, Hamburg, Germany
[i] Atmospheric Science and Global Change Division, Pacific Northwest National Laboratory, Richland, Washington

ABSTRACT

Changes in precipitation characteristics directly affect society through their impacts on drought and floods, hydro-dams, and urban drainage systems. Global warming increases the water holding capacity of the atmosphere and thus the risk of heavy precipitation. Here, daily precipitation records from over 700 Chinese stations from 1956 to 2005 are analyzed. The results show a significant shift from light to heavy precipitation over eastern China. An optimal fingerprinting analysis of simulations from 11 climate models driven by different combinations of historical anthropogenic (greenhouse gases, aerosols, land use, and ozone) and natural (volcanic and solar) forcings indicates that anthropogenic forcing on climate, including increases in greenhouse gases (GHGs), has had a detectable contribution to the observed shift toward heavy precipitation. Some evidence is found that anthropogenic aerosols (AAs) partially offset the effect of the GHG forcing, resulting in a weaker shift toward heavy precipitation in simulations that include the AA forcing than in simulations with only the GHG forcing. In addition to the thermodynamic mechanism, strengthened water vapor transport from the adjacent oceans and by midlatitude westerlies, resulting mainly from GHG-induced warming, also favors heavy precipitation over eastern China. Further GHG-induced warming is predicted to lead to an increasing shift toward heavy precipitation, leading to increased urban flooding and posing a significant challenge for mega-cities in China in the coming decades. Future reductions in AA emissions resulting from air pollution controls could exacerbate this tendency toward heavier precipitation.

1. Introduction

Precipitation is an important component of Earth's hydrological and energy cycles (Trenberth et al. 2007). Almost all water supplies that sustain terrestrial ecosystems, agriculture, and human life come from precipitation; however, precipitation can also be damaging. Too much heavy precipitation and too little light precipitation can cause severe flooding and drought, respectively, both of which can cause devastating damages to agriculture,

infrastructure, and human life (IPCC 2012). Because of this, potential changes in precipitation "characteristics" in climate projections and observations have been a key subject of research (e.g., Allen and Ingram 2002; Trenberth et al. 2003; Lau and Wu 2007; Sun et al. 2007; IPCC 2007, 2013; Liu et al. 2009; Pall et al. 2011; Shiu et al. 2012; Lau et al. 2013).

There are many causes of changes in precipitation. The leading cause is the increase in atmospheric water vapor content associated with rising air temperatures. Atmospheric water vapor increases roughly at the Clausius–Clapeyron rate of 7% K^{-1} based on theoretical arguments (Trenberth et al. 2003), observations (Trenberth

Corresponding author e-mail: Dr. Tianjun Zhou, zhoutj@lasg.iap.ac.cn

et al. 2005; Dai 2006a; Willett et al. 2010; Zhao et al. 2012), and model simulations (Held and Soden 2006; Pall et al. 2007; Sun et al. 2007). In response to greenhouse gas (GHG)-induced global warming, climate models project that global mean precipitation will increase at rate of 1%–3% K^{-1} (IPCC 2007, 2013; Held and Soden 2006; Sun et al. 2007). This reduced increase in global mean precipitation relative to the increase in water vapor is a result of the surface and atmospheric energy constraints on global mean precipitation rates (Allen and Ingram 2002; Pendergrass and Hartmann 2014). Trenberth et al. (2003) argued that precipitation intensity from storms is likely to increase with the increasing rate of water vapor (~7% K^{-1}), which implies that precipitation frequency should decrease. This thermodynamic argument has roughly held true in many subsequent analyses of climate model projections (e.g., Sun et al. 2007; Chou et al. 2012; Lau et al. 2013) and historical data (e.g., Goswami et al. 2006; Qian et al. 2007; Allan and Soden 2008; Liu et al. 2009; Shiu et al. 2012; Lau and Wu 2007; Westra et al. 2013; Ma et al. 2015).

Another cause of precipitation change is anthropogenic aerosols (AAs), which can impact precipitation characteristics through complex aerosol–cloud–climate interactions and through the scattering and absorption of incoming solar radiation (Rosenfeld et al. 2008; Lee et al. 2014). In addition to their effects in the troposphere, aerosols cool the surface, which offsets the GHG-induced warming and thus its impact on precipitation (Mitchell et al. 1995; Chen et al. 2011). Anthropogenic aerosols have been found to weaken the South Asian summer monsoon (Bollasina et al. 2011) and to cause a tendency for global dry land regions to become wetter and wet regions to become drier during the second half of the twentieth century (Sun et al. 2012). Anthropogenic aerosols have had a detectable contribution to the decrease in monsoon precipitation in the Northern Hemisphere (Polson et al. 2014) and the weakening of the hydrological cycle between the 1950s and the 1980s (P. Wu et al. 2013). AA loading over eastern China (EC) has been among the highest in the world during the last several decades due to the rapid economic development in the region. Previous studies suggest that AA are partly responsible for the summer "southern flood and northern drought" trend over EC associated with the weakening of summer monsoon circulation (Jiang et al. 2013; Ye et al. 2013; L. Wu et al. 2013; Song et al. 2014) and recent changes in precipitation characteristics over EC (Qian et al. 2009; Fu and Dan 2014).

High-impact floods and droughts are closely related to the tail behavior of the frequency and amount distributions of daily precipitation (Goswami et al. 2006). Light and heavy precipitation events, which are, respectively, closely related to drought (Dai 2011, 2013) and floods (Dai 2016), are likely to be more sensitive to anthropogenic emissions than the mean precipitation amount (Trenberth et al. 2003; Sun et al. 2007; Westra et al. 2013; Zhao and Dai 2015). The human-induced GHG increases have had a detectable effect on the observed intensification of extreme heavy precipitation during the second half of the twentieth century (Min et al. 2011; Zhang et al. 2013) and the observed intensification of the hydrologic cycle after the 1980s (Polson et al. 2013; P. Wu et al. 2013). Nonetheless, the detection of regional precipitation change has been a challenge outside of the Arctic (Min et al. 2008), and whether anthropogenic climate change is manifested through a detectable effect on East Asian precipitation remains unknown.

In this study, we investigate the influences of historical GHG, AA, and other climate forcing agents on the observed changes in the amount distributions of daily precipitation over EC from 1956 to 2005 and by comparing them to those simulated by climate models. Optimal fingerprinting (Allen and Stott 2003), which is widely used in detection and attribution studies (Polson et al. 2013, 2014; Min et al. 2011; P. Wu et al. 2013; Zhang et al. 2013), is employed to further determine whether the observed changes in the amount distributions of EC precipitation have been caused by external forcings and are thus detectable. In addition, because of the greater contribution of internal variability and greater errors in climate models' representation of regional details at smaller spatial scales (IPCC 2013), it become more difficult to detect and attribute the change precipitation amount distribution at smaller spatial scales. Meanwhile, as indicated in previous study (Liu et al. 2015), the compensation effect with large spatial averaging (entire eastern China region) is neither a common nor a serious problem, but rather the sporadic nature of precipitation makes it difficult to derive a significant signal when data from a very limited number of station are used. Thus, the detection and attribution analyses on changes in the distribution of the daily precipitation amount were focused on eastern China as a whole. Finally, the possible physical mechanisms between the external forcings and the changes in daily precipitation over EC are explored.

The remainder of the paper is organized as follows. Section 2 describes the data and method used in the study. The results of the study are given in section 3. Major findings are summarized in section 4 along with a discussion.

2. Data and method

a. Data description

Rain-gauge data of daily precipitation from 1956 to 2005 were obtained from the China Meteorological

TABLE 1. Details of the 11 CMIP5 models used in the study. AA forcing agents are defined as follows: C is 3D aerosol distributions specified as monthly 10-yr mean aerosol concentrations, derived using the CAM–Chemistry model, which is driven by Lamarque et al. (2010); AAs include organic carbon (OC), black carbon (BC), and sulfur dioxide (SO_2). E1 is AA emissions taken from Lamarque et al. (2010). E2 is the same as E1, but with BC increased uniformly by 25% and organic aerosol increased by 50% (Rotstayn et al. 2012). SD is anthropogenic sulfate aerosol accounting only for direct effects. SA is anthropogenic sulfate aerosol accounting for both direct and indirect effects. (Acronym expansions are available online at http://www.ametsoc.org/PubsAcronymList.)

	Model name	Horizontal resolution (lat × lon grid points)	Institute	Anthropogenic aerosol forcing agents	Aerosol effects
1	CanESM2	64 × 128	Canadian Centre for Climate Modelling and Analysis, Canada	E1	SA
2	CCSM4	192 × 288	National Center for Atmospheric Research, United States	C	SD
3	CESM1(CAM5)	192 × 288	NSF–DOE–NCAR, United States	E1	SA
4	CNRM-CM5	128 × 156	Centre National de Recherches Météorologiques and Centre Européen de Recherches et de Formation Avancée en Calcul Scientifique, France	E1	SA
5	CSIRO Mk3.6.0	96 × 192	Commonwealth Scientific and Industrial Research Organisation–Queensland Climate Change Centre of Excellence, Australia	E2	SA
6	GFDL CM3	90 × 144	NOAA/GFDL, United States	E1	SA
7	GFDL-ESM2M	90 × 144	NOAA/GFDL, United States	E1	SD
8	HadGEM2-ES	145 × 192	Met Office Hadley Centre, United Kingdom	E1	SA
9	IPSL-CM5A-LR	96 × 96	L'Institut Pierre-Simon Laplace, France	E1	SA
10	MIROC-ESM	64 × 128	Atmosphere and Ocean Research Institute, National Institute for Environmental Studies, and Japan Agency for Marine-Earth Science and Technology, Japan	E1	SA
11	NorESM1-M	96 × 144	Norwegian Climate Centre, Norway	E1	SA

Administration (CMA; http://data.cma.cn/en). The CMA dataset contains 756 stations and is updated through recent years; we used data only up to 2005 to be consistent with the available climate model historical simulations, which end in 2005. After excluding those stations whose site may have been changed or whose record lengths is insufficient, we retained 436 stations over EC (approximately 18°–43°N, 100°–125°E) in our calculations. Monthly precipitable water and atmospheric column water vapor flux data obtained from the Japanese 55-year Reanalysis (JRA-55; Ebita et al. 2011) were also used.

We used a total of 147 simulations from historical experiments performed by 11 models from phase 5 of the Coupled Model Intercomparison Projection (CMIP5, see Tables 1 and 2; Taylor et al. 2012). Here, we considered five groups in the historical climate simulations. These include simulations forced with 1) estimates of changes in all important external forcings (ALL forcings), which combines anthropogenic (greenhouse gases, aerosols, land use, and ozone) and natural (volcanic and solar) forcings, 2) anthropogenic-only forcing (ANT forcing), 3) GHG-only forcing (GHG forcing), 4) anthropogenic aerosol-only forcing

(AA forcing), and 5) natural-only forcing (NAT forcing). The composition of each group and the ensemble size of the simulations of each model are listed in Table 2. The preindustrial control simulations (CTL) were also used to estimate natural internal variability in the climate models.

b. Calculation of precipitation characteristics

As in Ma et al. (2015), for a given station (grid) and year (season), precipitation frequency in each intensity interval is the ratio (in percent) of the number of days whose daily precipitation rate is within the corresponding intensity interval to the number of all days with data; the precipitation amount in each intensity bin is the accumulated precipitation amount over the precipitation days within the corresponding intensity interval. To estimate the regionally averaged precipitation amount and frequency at each intensity interval, at each station and model grid, the annual (seasonal) precipitation amount and frequency at each intensity bin were calculated. Then, for the observations, the station annual (seasonal) precipitation amount and frequency of each intensity bin were interpolated onto a 0.5° × 0.5° grid using the iterative improvement objective analysis (NCAR 2012), and these 0.5° grid cells were averaged

TABLE 2. Information on the number of simulations in the five historical experiments forced by ALL, ANT, GHG, AA, and NAT forcing. The lengths of the CTL runs and the number of simulations for the representative concentration pathway 8.5 (RCP8.5) projection are also included.

Model	ALL ensemble size (runs)	ANT ensemble size (runs)	GHG ensemble size (runs)	AA ensemble size (runs)	NAT ensemble size (runs)	CTL (yr)	RCP8.5 ensemble size (runs)
CanESM2	5	—	5	5	5	1096	1
CCSM4	5	4	3	3	4	156	1
CESM1(CAM5)	1	—	—	3	2	—	1
CNRM-CM5	10	10	6	—	6	500	1
CSIRO Mk3.6.0	10	5	5	5	5	850	1
GFDL CM3	5	3	3	3	3	800	1
GFDL-ESM2M	1	1	1	1	1	500	1
HadGEM2-ES	5	—	4	—	4	575	1
IPSL-CM5A-LR	6	3	3	1	3	1000	1
MIROC-ESM	3	—	3	—	3	630	1
NorESM1-M	3	—	3	1	1	201	1
Sum	11 models, 54 runs	6 models, 26 runs	10 models, 34 runs	8 models, 22 runs	11 models, 37 runs	10 models	11 models, 11 runs

using the area as weight to calculate regional averages for each intensity bins. For simulations, for each bin, annual area-weighted means were computed on the original model grid cells over each bin, and the multi-model ensemble mean (MME) was calculated by first calculating ensemble means from individual models and then averaging over the available models.

For example, to obtain the long-term mean histograms of daily precipitation amount and frequency over eastern China (shown in Fig. 1), at each station and grid, daily precipitation was divided into 100 intensity bins with a bin size of $1\,\mathrm{mm\,day}^{-1}$, and the annual precipitation amount, and frequency at each intensity bin were calculated. Then observed regionally averaged precipitation amount and frequency at each bin were calculated after the station annual precipitation amount and frequency were interpolated onto a 0.5° grid (for other grids, such as 1.5° and 2.5°, the methods of calculating regional averages were similar and figures are not shown). The simulated regionally averaged precipitation amount and frequency at each bin were calculated on the individual model's original grids and then the multimodel ensemble mean was calculated.

The current GCMs tend to produce too much light and moderate precipitation while missing most heavy and extreme precipitation events (Fig. 1). Thus, when investigating the changes in the distributions of frequency and of amounts of daily precipitation over eastern China, following previous studies (Allan et. al. 2010; Chou et al. 2012; Shiu et al. 2012), first, the observed and historical simulated daily precipitation data at each station and model grid over eastern China were ranked from light to heavy for the period 1956–2005, respectively, and then 20 precipitation intensity bins at each station and model grid were calculated by dividing

the long-term mean histograms of precipitation amount into 20 bins with equal amount of precipitation. These 20 intensity bins were used to calculate histograms of precipitation amounts at each observational station and model grid for individual years, and then the area-weighted averages were calculated. The ranges of each percentile bin regionally averaged over eastern China
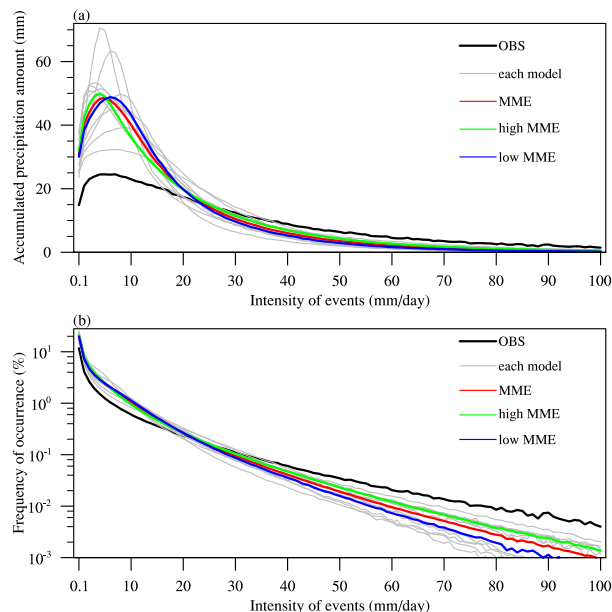

FIG. 1. Long-term (1956–2005) mean annual histograms of yearly (a) accumulated precipitation amount (mm) and (b) frequency of occurrence (%) as a function of daily precipitation intensity from 0.1 to $100\,\mathrm{mm\,day}^{-1}$ (bin size is $1\,\mathrm{mm\,day}^{-1}$), averaged over EC. The thick black lines are for the observations. The thick red, green, and blue lines are for MME of the historical simulations from 11 models, 5 high-resolution models, and 6 low-resolution models, respectively. The thin gray lines are for individual model ensemble means.

TABLE 3. Ranges of the 20 bins with equal total precipitation amounts (mm day^{-1}) corresponding to the observations (OBS) and 11 CMIP5 models. Each bin or range has a lower and upper limit. Shown here are the upper limits of bins 1–19 and the lower limit of bin 20; the lower limit for bin 1 is 0.1 mm day^{-1}.

Bin	1	2	3	4	5	6	7	8	9	10	11	12	13	14	15	16	17	18	19	20
OBS	2.5	4.5	6.5	8.5	10.5	12.7	15	17.5	20.2	23.2	26.5	30.3	34.6	39.7	46.1	54.0	64.8	81.1	111.4	≥111.4
CanESM2	1.8	3.2	4.4	5.4	6.4	7.3	8.3	9.3	10.5	12.0	13.8	16.2	19.1	22.6	26.5	31.4	37.4	46.0	60.9	≥60.9
CCSM4	1.4	2.5	3.6	4.8	6.0	7.2	8.5	10.2	11.7	13.6	15.4	18.0	20.8	23.8	28.1	32.8	39.5	49.5	67.8	≥67.8
CESM1(CAM5)	1.4	2.7	4.0	5.2	6.5	7.8	9.1	10.5	12.1	13.8	15.7	17.9	20.5	23.6	27.4	32.2	38.6	47.8	64.6	≥64.6
CNRM-CM5	1.8	2.8	3.7	4.6	5.4	6.3	7.0	8.0	9.3	10.7	12.5	14.3	16.7	20.3	24.0	29.4	36.6	47.1	66.7	≥66.7
CSIRO Mk3.6.0	1.7	3.4	4.9	6.5	8.0	9.6	11.3	12.9	14.6	16.4	18.4	20.4	22.7	25.3	28.2	31.7	36.0	41.8	51.2	≥51.2
GFDL CM3	1.2	2.3	3.3	4.3	5.3	6.3	7.4	8.5	9.7	11.0	12.4	14.0	15.8	18.0	20.6	24.0	28.3	34.4	44.9	≥44.9
GFDL-ESM2M	1.8	3.2	4.5	5.7	6.9	8.1	9.3	10.6	11.8	13.2	14.6	16.2	18.1	20.4	23.2	27.4	33.5	43.0	60.7	≥60.7
HadGEM2-ES	1.4	2.5	3.6	4.8	6.0	7.2	8.6	10.1	11.8	13.7	15.8	18.3	21.2	24.7	29.0	34.6	42.0	52.6	70.6	≥70.6
IPSL-CM5A-LR	1.6	3.0	4.2	5.3	6.3	7.3	8.3	9.3	10.2	11.3	12.4	13.6	15.0	16.7	18.9	21.9	26.4	33.4	46.5	≥46.5
MIROC-ESM	1.6	3.0	4.4	5.7	7.0	8.3	9.5	10.8	12.1	13.5	14.9	16.5	18.2	20.2	22.5	25.4	29.1	34.6	43.9	≥43.9
NorESM1-M	1.5	2.6	3.8	4.9	6.1	7.4	8.7	10.0	11.5	13.1	14.8	16.7	18.8	21.1	23.9	27.3	31.6	37.5	47.2	≥47.2

were listed in Table 3. Thus, the regionally averaged histograms of the precipitation amount created here contain both temporal and spatial variations. For instance, the regionally averaged 95th percentile bin indicates the strongest percent of precipitation in the time–space cumulative distribution. Finally, changes in the regionally averaged amount distribution of daily precipitation intensity as a function of 20th percentile intensity bins were calculated using linear least squares fits (Fig. 2).

c. Total least squares detection method

The optimal fingerprinting approach pioneered by Hasselmann (1979, 1993), a frequently used method in the detection and attribution analysis, is applied to the multimodel ensemble mean and observed trends to determine if external forcings caused the changes. Similar to the methods used in previous studies (Zhang et al. 2007; Polson et al. 2013), the "optimal fingerprint" method used here (http://www.csag.uct.ac.za/~daithi/idl_lib/detect/, version 3.1.2) assumes that the observed trend **y** (a rank-n vector, where n is the number of daily precipitation intensity bins, with $n = 20$ used in this analysis) can be represented via generalized total least squares fitting as the sum of fingerprints or anomalous signals **X** (model simulated climate responses to external forcings, a matrix with one column for each external climate forcing), that is, $\mathbf{y} = \boldsymbol{\beta}(\mathbf{X} - \boldsymbol{v}) + \boldsymbol{\mu}$ (Allen and Stott 2003). The term $\boldsymbol{\mu}$ is the sampling error (i.e., noise) of **y** from the true anomalous response function underlying the real world, while $\boldsymbol{v}$ represents the same for the climate model responses sampled from a small number of simulations. Two independent estimates of the internal variability covariance structure needed for the optimization and uncertainty analysis are estimated from the preindustrial control simulations and intraensemble differences.

In this study, optimal fingerprinting is used for the analysis in the direction of maximum signal-to-noise

rather than in the direction of highest signal. A principal component analysis is performed on the first estimate of internal variability covariance; for this analysis, all data are projected onto this space and divided by the square root of the respective eigenvalues. Since weaker principal components need to be removed to avoid extreme amplification of the projection onto poorly sampled
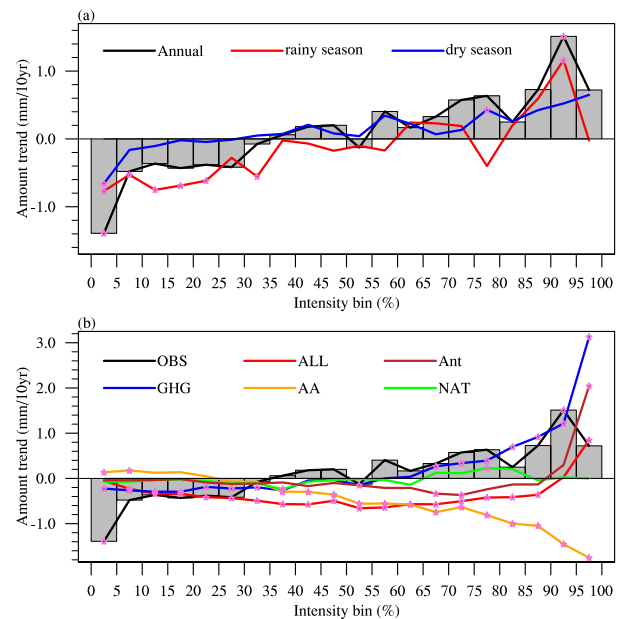

FIG. 2. Linear trend in precipitation amount as a function of 20 precipitation percentile intensity bins with equal total precipitation amount averaged over EC from 1956 to 2005, (a) observed trends in rainy (red) and dry (blue) seasons. (b) Simulated trends of annual precipitation amount derived from the MME of all external forcings (red), anthropogenic forcing (brown), greenhouse gas forcing (blue), anthropogenic aerosol forcing (orange), and natural forcing (green) simulations, respectively. Gray bars and black lines in (a) and (b) are for annual precipitation amount in the observations. Trends that are statistically significant at the 0.05 level of a two-tailed Student's t test are marked by purple stars.

patterns of variability, we truncate the data to the leading 16 empirical orthogonal functions (EOFs), determined by a residual consistency check (Allen and Stott 2003), and ensure that the regression residual is generally consistent with the simulated noise estimates. More than 78% of signal and noise variance is retained at this truncation. If the scaling factors $\boldsymbol{\beta}$ are positive and significantly inconsistent with zero at the one-sided 5% significance level, then the simulated fingerprint response patterns to the corresponding forcing are detectable in the observations. If the scaling factors are inconsistent with zero and consistent with unity, then the model-simulated response patterns are consistent with the observed changes. As models may underestimate precipitation variability, the uncertainty ranges of the scaling factors were checked for robustness against a doubling of the model noise variance (Zhang et al. 2007; Polson et al. 2013, 2014).

d. Moisture budget analysis

To understand what specific processes are responsible for the changes in precipitation amount, we examine a vertically integrated moisture budget equation as in Chou and Lan (2012):

$$P' = -\langle \mathbf{V}_h \cdot \nabla q \rangle' - \langle \omega \partial_p q \rangle' + E' + \delta'. \quad (1)$$

In Eq. (1), P is precipitation, E is evaporation, $-\langle \mathbf{V}_h \cdot \nabla q \rangle$ is horizontal moisture advection, $-\langle \omega \partial_p q \rangle$ is vertical moisture advection and is also referred to as the horizontal flow convergence of the moisture term (Seager et al. 2010), and δ is the residual term, which represents the transient eddies and contributions from surface processes due to topography. Primes denote departures from the climatology. The moisture convergence is usually the leading contributor to the changes of precipitation, and $-\langle \omega \partial_p q \rangle'$ can be further decomposed into three components: anomalous moisture convergence due to the changes in moisture $-\langle \overline{\omega} \partial_p q' \rangle$ (i.e., a thermodynamic effect), changes in circulation $-\langle \omega' \partial_p \overline{q} \rangle$ (i.e., a dynamic effect), and nonlinear contribution of both moisture and circulation changes $-\langle \omega' \partial_p q' \rangle$. As the nonlinear term is generally small and negligible, thus the changes of the vertical moisture advection can be further approximated as

$$-\langle \omega \partial_p q \rangle' \approx -\langle \overline{\omega} \partial_p q' \rangle - \langle \omega' \partial_p \overline{q} \rangle. \quad (2)$$

In Eq. (2), overbars and primes are climatology and departures from the climatology, respectively.

3. Results

To ascertain whether the observed changes in the distributions of EC precipitation amounts as a function

of daily precipitation intensity can be explained by internal climate variability alone or whether the external forcing has played a role in driving the observed changes, we first analyze the observed and simulated trends of precipitation amount in each precipitation intensity bin with the equal contribution to total precipitation amount. To facilitate discussion regarding precipitation characteristics in this study, the observed and simulated daily precipitation are defined by three major precipitation categories based on the empirical climatological histograms of daily precipitation amount over the period 1956–2005: the bottom 35% (light precipitation), moderate precipitation (within the range of 35%–90%), and the top 10% (heavy precipitation).

The 1956–2005 climatological histograms for daily precipitation amount and frequency for the individual model ensemble mean and MME are found to be similar in shape to the observations (Fig. 1). The station data show much lower frequencies and lower contributions for light-to-moderate precipitation ($<20\,\mathrm{mm\,day^{-1}}$) but higher frequencies and higher contributions for heavy to very heavy precipitation ($P > 35\,\mathrm{mm\,day^{-1}}$) than the model data, which are averaged precipitation rates over a grid box ranging from approximately 1.5° to 2.8° (Table 1). Some of these differences result from the different data resolutions, with the area-averaging in the model data reducing the local intensity of heavy precipitation, thereby shifting the frequency and amount distributions of daily precipitation intensity toward more light–moderate events. Nevertheless, this model bias is consistent with the "drizzling problem" found in previous studies (e.g., Dai 2006b; Sun et al. 2007). Despite these quantitative differences, all models show a gamma-like distribution of precipitation amount with a peak around the intensity of $4.0–10.0\,\mathrm{mm\,day^{-1}}$ and a long tail toward high precipitation intensity (Fig. 1a). Additionally, the frequency decreases rapidly with increasing daily precipitation intensity (Fig. 1b). These basic features are consistent with the observations.

The changes in precipitation characteristics are analyzed based on the linear trends in the shape of the annual distributions of the daily precipitation amount during the whole year, as measured with 20 precipitation intensity bins, each with an equal amount of precipitation (Fig. 2). The locations of the bins are determined separately for each dataset (method details of the calculation of precipitation characteristics are described in section 2b). The ranges of the 20 bins in the observations and simulations are given in Table 3. The observations (black lines and gray bars in Fig. 2) clearly show a decreasing trend for events with daily precipitation intensity below the 35th percentile and an increasing trend for events above the 55th percentile

averaged over eastern China. Given the strong influence of the East Asian monsoon on the precipitation in China, the observed shift of the distribution of precipitation amount during the rainy season (from April to September) and dry season (from October to the next March) are also calculated. As shown in Fig. 2a, the characteristics of decreased light precipitation and increased heavy precipitation are evident in the changes in the distribution of precipitation amount in both the rainy season and dry season. So the observed shifting of the daily precipitation amount distribution toward heavy precipitation is not seasonally dependent, consistent with previous study (Jiang et al. 2014), which suggests the observed percentage magnitude of daily precipitation frequency shifting from light to precipitation is more obvious in winter than summer. Thus, in the following analysis, we only focus on the changes in the annual distribution of the daily precipitation amount during the whole year.

The MMEs for the GHG forcing simulations show a tendency toward more intense precipitation amounts over EC, whereas the AA forcing simulations exhibit an approximately opposite change in the distributions of precipitation amount, with large decreases in heavy precipitation and slight increases in light precipitation. Although the AA effect partly offsets the shift in the amount distributions of daily precipitation toward heavier precipitation under GHG forcing, we witness a relatively reasonable match in the long-term changes in the shape of the daily precipitation amount distribution between the observed trends and the responses to ALL forcing, or between the observations and responses to ANT forcing, with the shift toward heavier precipitation mainly occurring in the top 10% precipitation intensity bins. We note that the NAT forcing simulations show a weak tendency in the precipitation amount distribution to shift from weak precipitation events to intense precipitation events, but the observed trends for all precipitation intensity bins are clearly larger than the model-simulated response to NAT forcing. The general consistency in the changes of the precipitation amount distribution between the observations and the ALL, ANT, and GHG forcing ensemble simulations over EC implies that the observed shift in the distribution of daily precipitation amount is closely related to the anthropogenic climate forcings.

Quantitatively, the observed bottom 35% light precipitation averaged over EC shows a statistically significant decreasing trend of -3.5 mm decade^{-1} at the 5% level (two-tailed Student's t test), whereas the top 10% heavy precipitation exhibits an increasing trend of 2.3 mm decade^{-1}, which is statistically significant at the 0.05 level (Figs. 3 and 4). The amount of precipitation
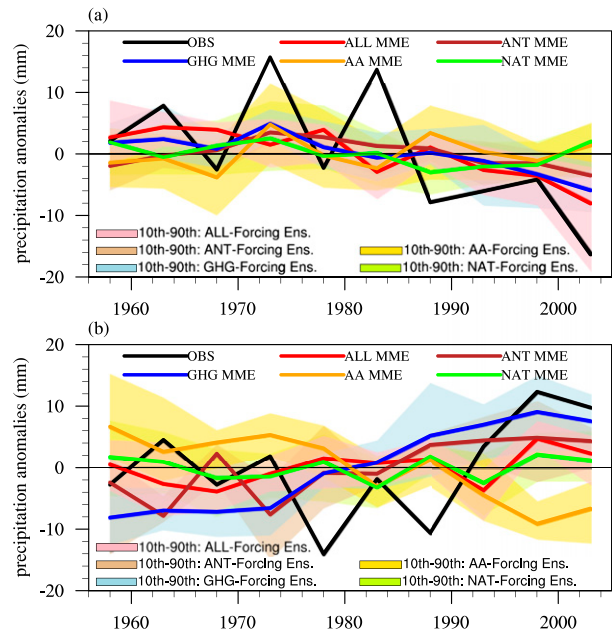

FIG. 3. Five-year mean precipitation amount anomalies (mm) from 1956 to 2005 for the (a) bottom 35% light precipitation and (b) top 10% heavy precipitation averaged over EC. Anomalies are with respect to the mean for 1956–2005. Black lines are for the observations. The other colored lines are for the MME of the ALL (red lines), ANT (brown lines), GHG (blue lines), AA (orange lines), and NAT (green lines) forcing simulations, respectively. The light pink, light brown, light blue, yellow, and green shadings show the 10%–90% range of the ALL, ANT, GHG, AA, and NAT forcing ensembles, respectively.

associated with moderate precipitation events over EC also shows an increasing trend of 2.4 mm decade^{-1}, but is not significant at the 0.1 level (figure not shown).

Spatially, observed bottom 35% light precipitation exhibits a regionally consistent decreasing trend over EC (Fig. 5). As expected, given the overall increase in daily precipitation amount, the predominantly decreasing trends over EC for light precipitation is matched by predominantly increasing trends at higher intensities (Fig. 5). The simulations, including GHG forcing, generally show similar behavior as the observations in the time series and trend patterns for the bottom 35% light precipitation and top 10% heavy precipitation, respectively (Figs. 3 and 5), suggesting that the observed decrease in light precipitation and increase in heavy precipitation mainly come from the contribution of GHG forcing. Anthropogenic aerosols partly offset the contribution of GHGs. Based on the trend estimates for the area-weighted average over EC, observations and MME of ALL, ANT, GHG, and NAT forcing show a consistently decreasing trend in the bottom 35% light precipitation and increasing trend in the top 10% heavy precipitation, respectively (Figs. 3 and 4).
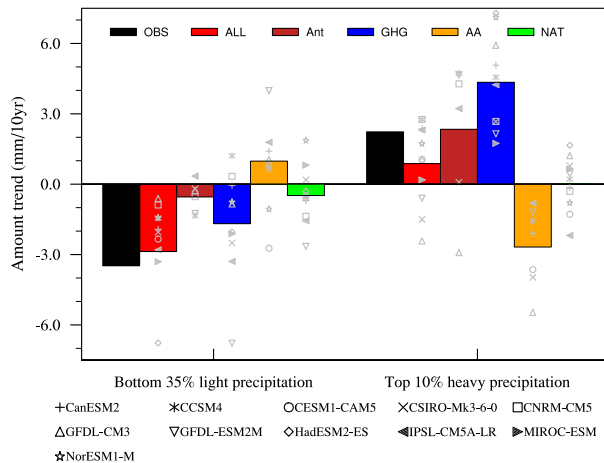
FIG. 4. Linear trends of precipitation amount (mm decade^{-1}) during 1956–2005 for the bottom 35% light precipitation at left and top 10% heavy precipitation at right averaged over EC. Black bars are for observations. Red, green, brown, orange, and green bars are for MME of the ALL, ANT, GHG, AA, and NAT forcing simulations, respectively. Gray symbols represent different models.

In the MME of AA forcing, the bottom 35% light precipitation and top 10% heavy precipitation amount exhibit an increasing and decreasing trend, respectively (Figs. 3 and 4). AA forcing has reduced the increase of moderate precipitation, cancelling out the positive contribution from GHG forcing and causing the decrease in moderate precipitation in the ALL and ANT forcing responses (Fig. 2). As indicated in Table 1, CCSM4 and GFDL-ESM2M include only the direct effect of aerosols, and the other nine modes include both the direct and indirect effects of aerosols. To tease out the indirect effect of aerosol, we have tried producing Fig. 5 for just the models that include the aerosol indirect effect. It is shown that the results derived from those models with aerosol indirect effects are similar with that of all available multimodel ensemble means (Fig. 6). The estimated contribution of NAT forcing to the observed changes in precipitation amount is negligible.

To determine the causes of the observed changes in the distribution of precipitation amount, we estimated the contributions of the individual external forcings to the observed precipitation trends by regressing the observed trends of the precipitation amount distribution onto the simulated distribution trends using the optimal fingerprint analysis. The regression vector consisted of the linear trends calculated for each of the 20 intensity bins. As shown in Fig. 6, the results confirm that external forcing has played a substantial role in driving the observed shift in the amount distribution of daily precipitation over EC. The fingerprint of ALL forcings is detected in the observations, and the model-simulated

responses of the precipitation amount distribution to ALL forcings are consistent with the observed shift, with the scale factor β significantly larger than zero and consistent with 1.

To ascertain which forcing components were dominant in driving the detected response, the observed trends of the 20 precipitation intensity bins were then regressed onto the ANT, GHG, AA, and NAT forcing responses separately (Fig. 7a). The scale factor β for ANT is consistent with 1 and the corresponding residual is consistent with internal variability, indicating that the responses to ANT forcing alone are detected in the observed shift in the amount distribution of daily precipitation. But the scale factor β for NAT forcing is significantly greater than 1 and the corresponding residual is not consistent with internal variability, suggesting either that the modeled response to NAT forcing is significantly underestimated compared to the observed response and cannot account for the observed shape in changes of the precipitation amount distribution or, more likely, that the response is strongly degenerate with the response to ANT forcing; both possibilities are consistent with the visual inspection of Fig. 2. Combined with the comparable magnitude and confidence interval of β between ALL and ANT forcing, it is concluded that ANT forcing is primarily responsible for the forced changes in the ALL fingerprint detected in the observations. Additionally, GHG forcing is detected in the observed changes, with β significantly larger than zero and passing the residual consistency test. Meanwhile, the scale factor β for GHG forcing is smaller than 1, suggesting that models overestimated the observed shift, consistent with the larger increases of the top 10% heavy precipitation amount in GHG forcing simulations than in observations (Fig. 4). However, the AA forcing response is not detected in the observed change, with the 90% confidence interval of β for AA forcing being negative (i.e., the shape of the change is opposite that of the observations). Consequently, it is concluded that the detected responses in ALL and ANT forcing are dominated by GHG forcing.

Single-signal regression neglects the possibility of correlation between signals; thus, to distinguish the influence of one forcing from the others, multisignal detection is needed. To ascertain the separately detectable influence of ANT forcing on the observed changes in the precipitation amount distribution from NAT forcing, two-signal analyses for ANT forcing and NAT forcing were performed (Fig. 7b, left-hand side). The detectable effect of ANT forcing can be separated from NAT forcing, with β inconsistent with zero for ANT forcing and significantly larger than one for NAT forcing and the successful passage of the corresponding residual
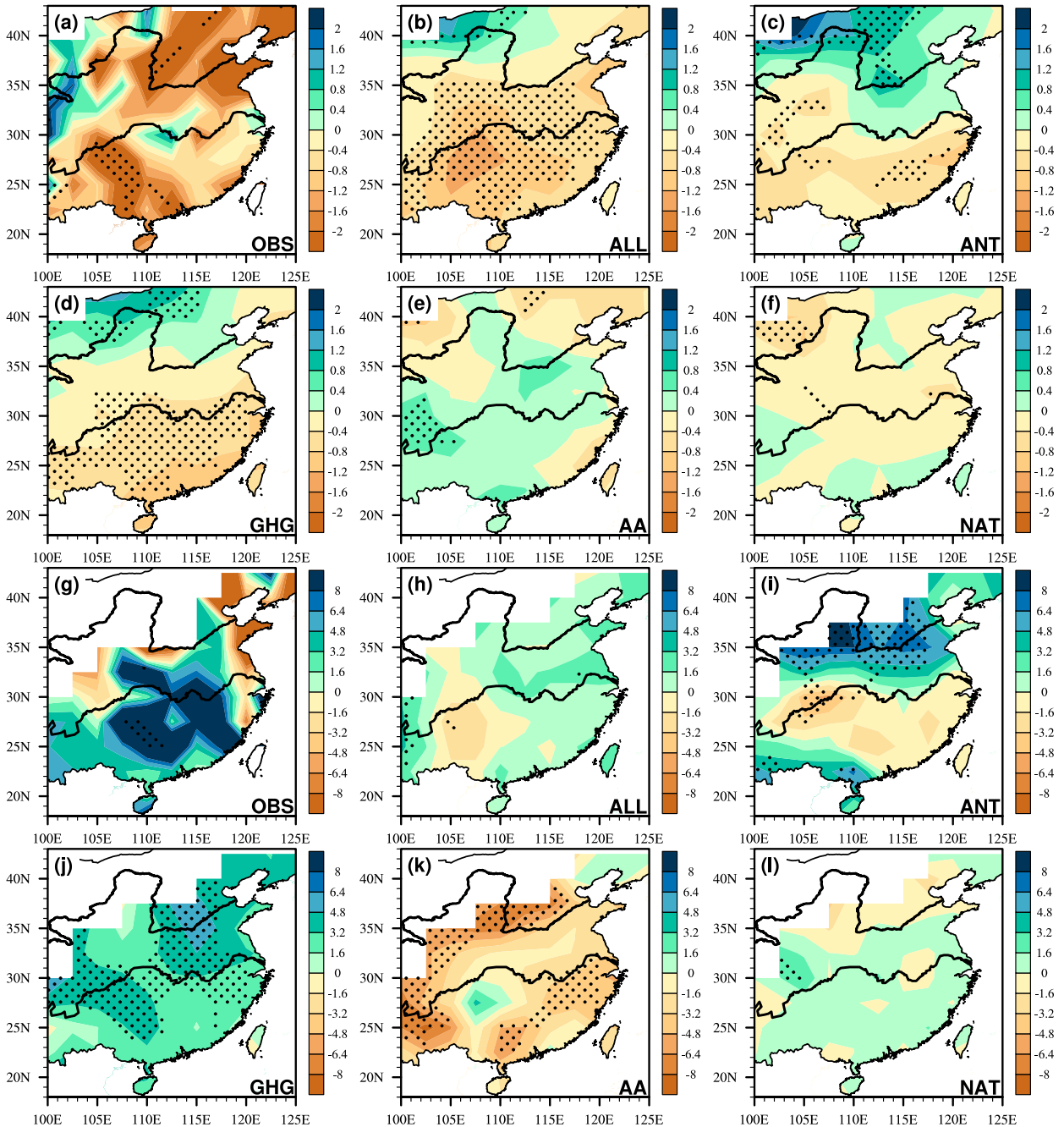
FIG. 5. Linear trends (% decade^{-1}) in precipitation amount from 1956 to 2005 over EC, for the bottom 35% light precipitation in the (a) observations and the MME of the (b) ALL, (c) ANT, (d) GHG, (e) AA, and (f) NAT forcing simulations. (g)–(l) As in (a)–(f), but for the top 10% heavy precipitation. The black dotted areas indicate that the trends in precipitation amount are statistically significant at the 0.1 level of a two-tailed Student's *t* test.

consistency test, although the large-scale factors on NAT indicate some model deficiencies in simulating observed changes. Nevertheless these results support the hypothesis that anthropogenic forcings has had a detectable influence on the observed daily precipitation amount distribution.

We now investigate whether we can further decompose the ANT forcing into different anthropogenic forcing factors. The ANT forcing is decomposed into GHG forcing and AA forcing and the two-signal analyses for GHG forcing and AA forcing was done (Fig. 7b, right-hand side). The result indicates that the
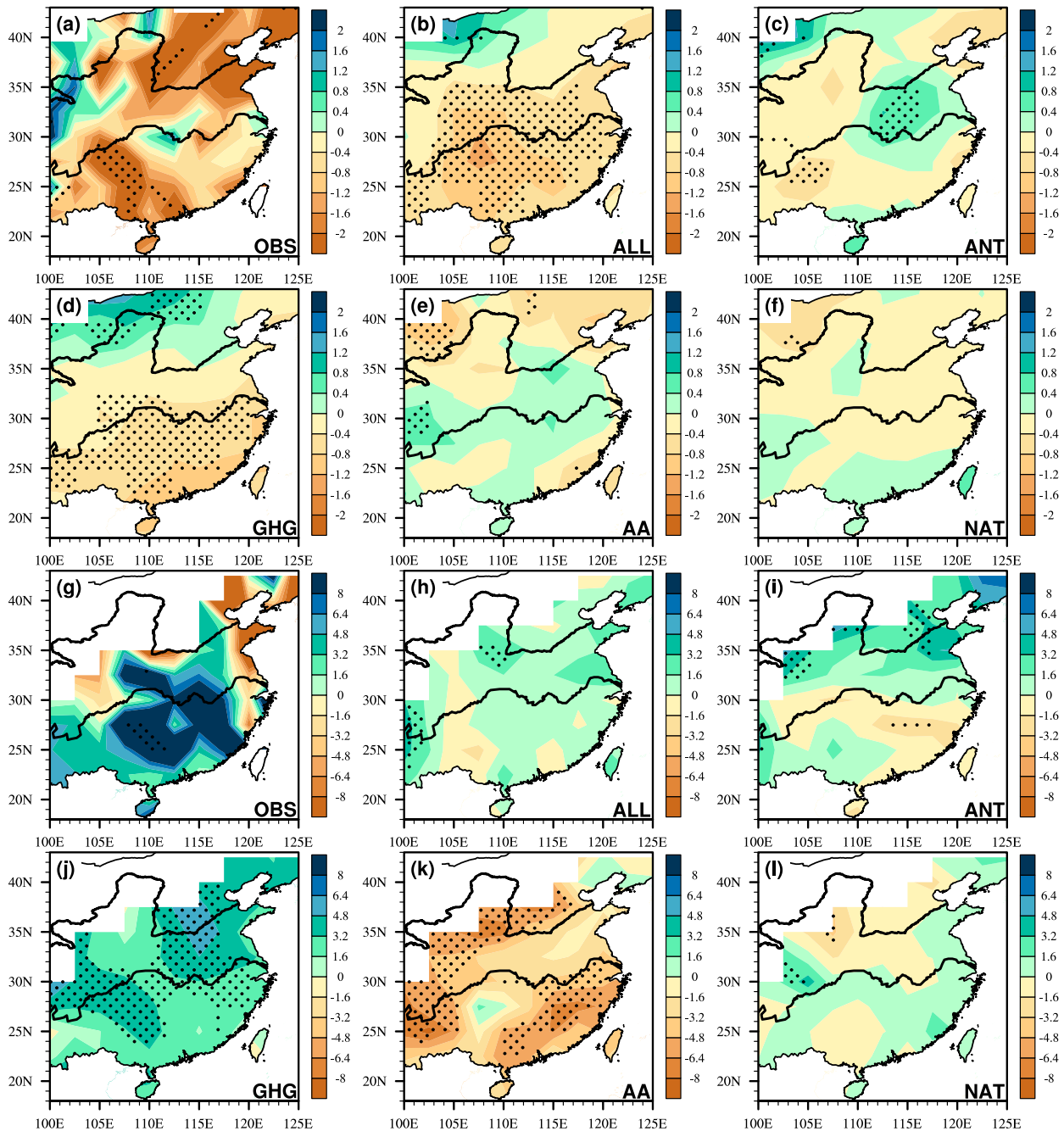
FIG. 6. As in Fig. 5, but for just the models that include the aerosol indirect effect.

GHG forcing is detected but the AA forcing is not and its magnitude is reduced to zero. The detectable influences of GHG forcing on the precipitation amount distribution still holds in the two-signal regressions and can be separated from AA forcing when the estimates of internal variance are doubled.

It is concluded that the detected shifts in the amount distribution of the observed daily precipitation intensity are likely largely in response to the overall effects of anthropogenic forcings. There is no clear evidence from the optimal detection results for the effects of aerosol forcing having offset the effects of greenhouse gas forcing, although degeneracy between the responses to greenhouse gas and aerosol response makes it difficult to distinguish between them in this way. While the scaling factors on ALL and ANT are consistent with 1 in a
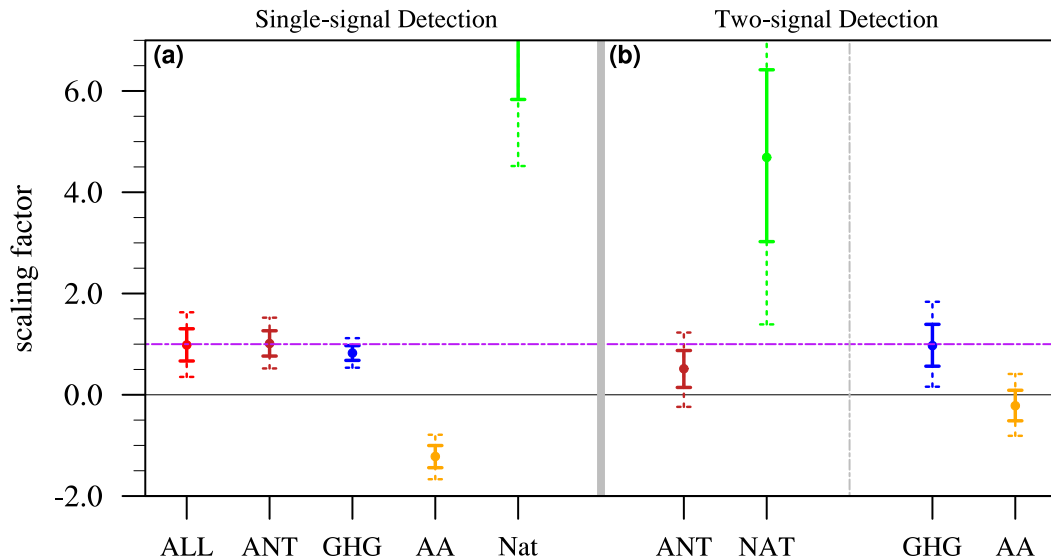
FIG. 7. Results from optimal detection analyses of changes in the distribution of precipitation amounts as a function of daily precipitation intensity bins over the period 1956–2005. (a) Single-signal regression coefficients of observed vs simulated changes in daily precipitation amount distribution for the ALL, ANT, GHG, AA, and NAT forcing. (b) Two-signal regression for ANT and NAT, GHG, and AA, respectively. Best estimates (dots) and 5%–95% uncertainty ranges (error bars) of regression coefficients β are displayed. Dotted error bars show 5%–95% uncertainty ranges of β when the internal variability is doubled. The residual consistency test is passed in all cases except NAT forcing in (a).

single-signal regression the scaling factor on GHG is significantly less than 1 (Fig. 7a), providing some support to the hypothesis that aerosol forcings have offset the greenhouse gas response. This hypothesis is now investigated further.

Precipitation over any land region is contributed by the water vapor carried from the surrounding areas and local evaporation, which has relatively small contribution; thus, anomalous precipitation is directly related to the moisture supply. There are three main moisture supply sources for the East Asia precipitation: a strong moisture transport by southwesterlies from the Bay of Bengal, another strong transport by southeasterlies from the western Pacific, and a weak transport from the South China Sea (Fig. 8). Moreover, northern EC is affected by a weak water vapor transport associated with the midlatitude westerlies. The water vapor transport brings the warm and sufficient moisture from the adjacent oceans and favors precipitation over EC, becoming one the most important components of the East Asian monsoon system (Zhou and Yu 2005).

In the GHG simulations, globally consistent warming (Fig. 9d) causes a significant increase in the atmospheric moisture content (Fig. 10b). The largest percentage increases of the precipitable water are centered over the western tropical Pacific and Eurasia, especially western China, where the surface air temperature also exhibit a larger warming than other regions. These simulated trends in precipitable water are similar to those observed

trends of previous studies (Dai 2006a; Durre et al. 2009). Additionally, the warming trends over land are stronger than those over adjacent oceans, enhancing the land–sea thermal contrast and leading to the strengthening of the
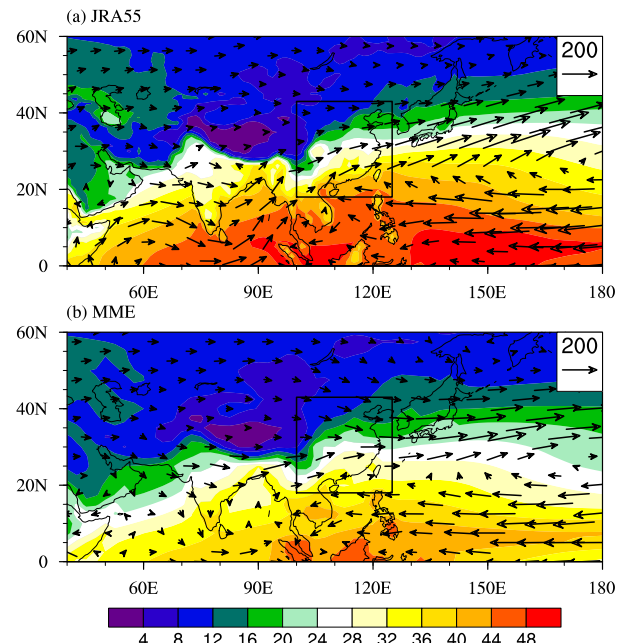

FIG. 8. Climatological distribution of atmospheric column precipitable water (shading; kg m^{-2}) and water vapor flux (vector; kg m s^{-1}) derived from (a) JRA-55 and (b) MME of historical simulations of all external forcings. The box indicates EC.
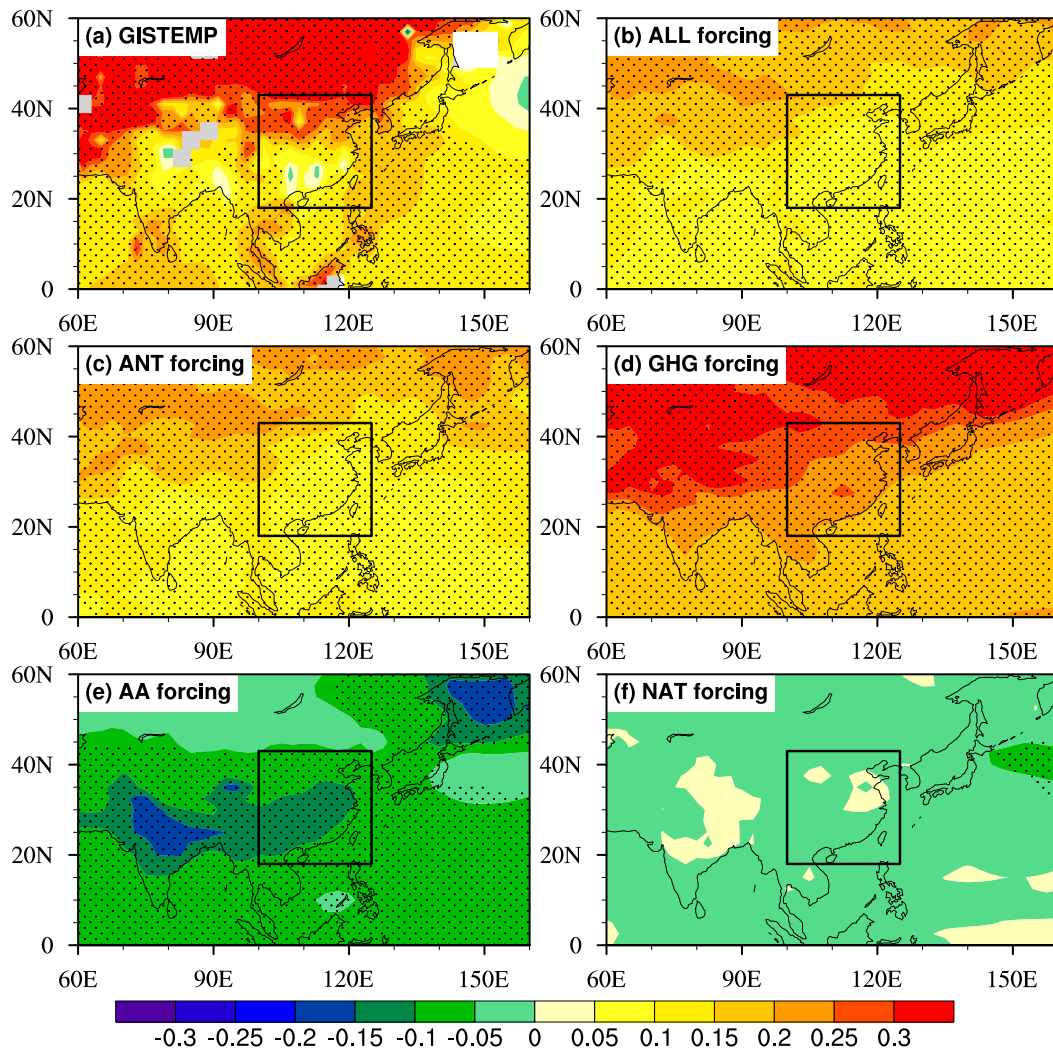
FIG. 9. Linear trends (shading; K decade^{-1}) of near-surface air temperature from 1956 to 2005 in (a) GISTEMP, (b) ALL, (c) ANT, (d) GHG, (e) AA, and (f) NAT forcing MME. The black dotted areas indicate that the corresponding trends are statistically significant at the 0.01 level of a two-tailed Student's t test. The box indicates EC.

climatological southerlies blowing from the western Pacific and Indian Oceans to China. Under the combined effects of increasing moisture and strengthening southerlies (i.e., the positive contribution of both the thermodynamic and dynamic effects; Fig. 11), the strengthening of moisture convergence dominates the increase of precipitation. Evaporation and horizontal moisture advection also contribute positively to the increase of precipitation but with smaller amplitude than the moisture convergence term (associated with the vertical moisture advection). The contribution from residual term is nearly negligible. Thus, the increased water vapor transport to EC from the Bay of Bengal, South China Sea, and western Pacific adds to the increased midlatitude westerlies' water vapor transport (Fig. 10b) and thereby is favorable for heavy precipitation over EC. In contrast, AA forcing induces

surface cooling (Fig. 9e) and a reduction in atmospheric water vapor (Fig. 10c); the stronger surface cooling over land than over adjacent oceans reduces the land–sea thermal contrast and leads to a weakening of the climatological southerlies. As a result of the negative contribution of both the thermodynamic and dynamic effects (Fig. 11), the decreased moisture convergence over EC (Figs. 10c and 11) is unfavorable for the occurrence of intense precipitation. The surface temperature shows insignificant change in the NAT forcing simulations. The surface warming pattern in the ALL and ANT forcing simulations and observations resemble that of GHG forcing (Fig. 8), but surface cooling induced by AA forcing offsets the increase in water supplies over EC, such that the water vapor transport in the ALL (and ANT) forcing simulations is weaker than those in the GHG
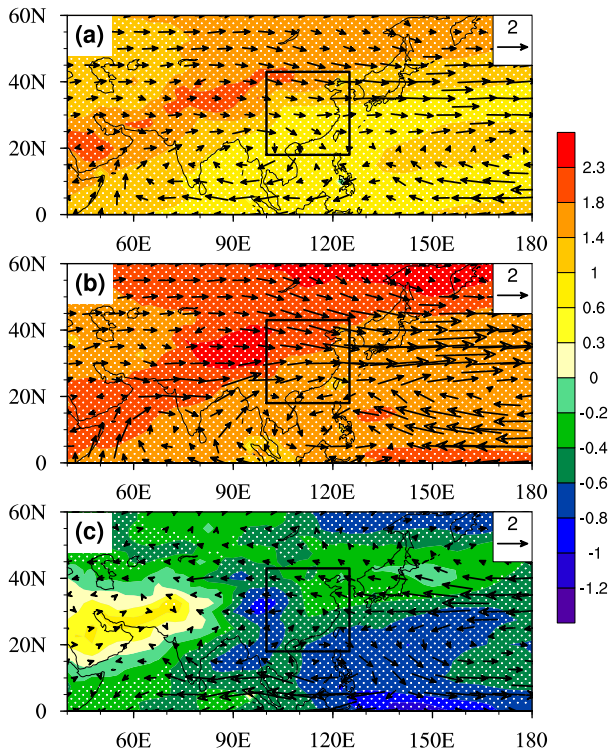
FIG. 10. Linear trends of atmospheric column precipitable water (shading; % decade^{-1}) and water vapor flux (vector; kg m s^{-1} decade^{-1}) in the (a) ALL, (b) GHG, and (c) AA forcing MME. The white dotted areas indicate that the trends of the convergence of the water vapor flux are statistically significant at the 0.1 level of a two-tailed Student's t test. The box indicates EC.

forcing simulations. Thus, the shift in the precipitation amount distribution from light precipitation to heavy precipitation under ALL (and ANT) forcing is weaker than that under GHG forcing.

4. Summary and discussion

a. Summary

In this study, the optimal fingerprinting analysis was performed on EC precipitation from 1956 to 2005 using CMIP5 historical simulations. We provide evidence for the first time that anthropogenic forcing has had a detectable and attributable influence on the distribution of daily precipitation amounts over EC during the second half of the twentieth century. We also provide some evidence that the observed shift from weak precipitation to intense precipitation is primarily due to the contribution of GHG forcing, with AA forcing offsetting some of the effects of the GHG forcing. The physical processes behind the observed shift in the amount distribution of the daily precipitation are clearly illustrated through investigation
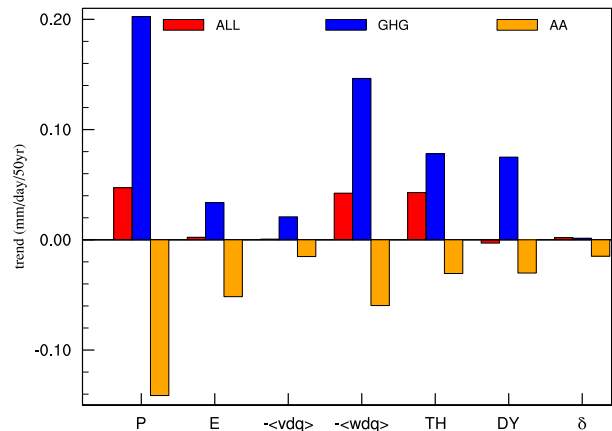

FIG. 11. Linear trends [mm day^{-1} (50 yr)$^{-1}$] of regionally averaged precipitation and each term of the moisture budget equation over EC in the MME of the ALL (red), GHG (blue), and AA (orange) forcing simulations. From left to right [see Eqs. (1) and (2)], P is precipitation, E is evaporation, $-\langle vdq \rangle$ is horizontal moisture advection, $-\langle wdq \rangle$ is vertical moisture advection, TH is the thermodynamic term, DY is the dynamic term, and δ is the residual term.

of the changes in water vapor supply simulated by the CMIP5 historical runs driven with different forcings. Under GHG-induced warming, increased atmospheric precipitable water and enhanced land–sea thermal contrast cause the water vapor transport to EC from the adjacent oceans via southerly and midlatitude westerly winds to strengthen, thereby favoring heavier precipitation over EC. However, the countering effects of surface cooling induced by anthropogenic aerosols meant that some of this enhanced transport is cancelled out by AA forcing.

b. Discussion

Based on the present study, both the detectable influences of the GHG and ANT forcing on the observed shift in the distribution of the daily precipitation amount toward intense precipitation are substantial, in agreement with the previous study (Liu et al. 2015), which also attributed primarily the observed decrease (increase) in light (heavy) precipitation in eastern China to global warming. The GHG-induced warming is likely to continue in the future, with the change in global surface temperature at the end of the twenty-first century likely to exceed 1.5°C relative to the present level for all representative concentration pathway (RCP) scenarios except RCP2.6 (IPCC 2013). This is set to cause increased shifts toward heavier precipitation. Because of the severe human health effects of polluted air caused by aerosol emissions, many countries around the world, especially China, have been reducing the emissions of sulfur aerosols (Wild

et al. 2008; Zhang et al. 2012). If the current efforts to reduce the emissions of aerosols and limit air pollution continue in the future, then this could cause even further shifts toward heavier precipitation over EC. In any event, further shifts toward heavier precipitation are expected as shown in the model projection under the RCP8.5 scenario (Fig. 12). The significant shift in precipitation to less light precipitation and more intense precipitation could pose major challenges to the management of the increased risks of severe floods and droughts.

One issue that is worthy of attention is why the inclusion of anthropogenic aerosols surprisingly makes the model results more inconsistent with the observed trends (see Figs. 2 and 4). This might be because current climate models do not have all the capacities needed to fully represent the multiple aerosol effects on precipitation. It is well known that anthropogenic aerosols from air pollution can affect precipitation via aerosol–radiation interaction (ARI) and aerosol–cloud interaction (ACI) effects (IPCC 2013). Solar radiation can be scattered and/or absorbed by aerosols via the ARI effect, which induces surface cooling and atmospheric heating and potentially enhances atmospheric static stability and suppresses rainfall (Menon et al. 2002; Ramanathan et al. 2005). Meanwhile, increased cloud condensation nuclei due to anthropogenic aerosols can also influence cloud microphysics and rainfall through the ACI effect; that is, as summarized in Qian et al. (2009), more aerosol particles lead to more cloud droplets but with smaller average drop size under identical ambient fields. In fact, Qian et al. (2009) found that cloud droplet number concentration is increased and cloud droplet size is reduced under heavily polluted conditions in eastern China, which results in a significant decline in raindrop concentration and a delay in raindrop formation because collision and coalescence are less efficient when cloud droplets are small.

In addition, as noted by Rosenfeld et al. (2008), suppression of precipitation by aerosols from shallow clouds may result in an increase in precipitation from deeper clouds at the cloud scale (Rosenfeld et al. 2008), the so-called aerosol invigoration effect. This has been demonstrated by some modeling studies that show that delay of early rain by aerosols can result in greater amounts of cloud water and rain intensities at the later stage of the cloud (Liu et al. 2002). This suggests that aerosols may increase the heavy storms and shift precipitation rates from light to moderate and heavy rains.

While the ARI effect is included in most of CMIP5 models we used in this study, only a very small number
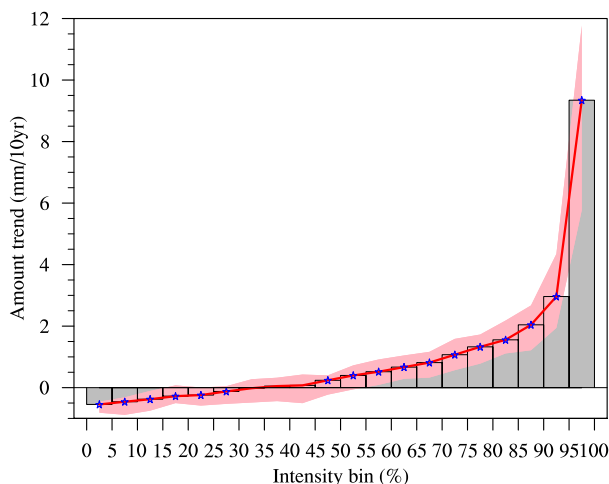

FIG. 12. Projections of the linear trend in precipitation amount (mm decade^{-1}) as a function of precipitation intensity bins averaged over EC from 2006 to 2100 for RCP8.5. Each precipitation bin (gray bars) contributes an equal proportion of the total precipitation amount. Red line is for the MME. The MME trends that are statistically significant at the 0.05 level of a two-tailed Student's t test are marked by stars. The assessed 10%–90% ranges for MME trends are shown as a light pink–shaded band.

of models fully or partially include the ACI effect, and none of models includes the aerosol invigoration effect, which implies that current climate models may not be able to fully capture the observed precipitation signals induced by aerosols.

Here, another issue that is worthy of attention is that the analysis in this study mainly focuses on the distribution of the daily precipitation amount throughout the year. However, the influences of GHGs and AAs could be different in different seasons because of different aerosol emission patterns and regional circulation.

National Laboratory is operated for DOE by Battelle Memorial Institute under Contract DE-AC05-76RL01830.

REFERENCES

Allan, R. P., and B. J. Soden, 2008: Atmospheric warming and the amplification of precipitation extremes. *Science*, **321**, 1481–1484, doi:10.1126/science.1160787.

——, ——, V. O. John, W. Ingram, and P. Good, 2010: Current changes in tropical precipitation. *Environ. Res. Lett.*, **5**, 025205, doi:10.1088/1748-9326/5/2/025205.

Allen, M. R., and W. J. Ingram, 2002: Constraints on future changes in climate and the hydrologic cycle. *Nature*, **419**, 224–232, doi:10.1038/nature01092.

——, and P. A. Stott, 2003: Estimating signal amplitudes in optimal fingerprinting, Part I: Theory. *Climate Dyn.*, **21**, 477–491, doi:10.1007/s00382-003-0313-9.

Bollasina, M. A., Y. Ming, and V. Ramaswamy, 2011: Anthropogenic aerosols and the weakening of the South Asian summer monsoon. *Science*, **334**, 502–505, doi:10.1126/science.1204994.

Chen, G., Y. Ming, N. D. Singer, and J. Lu, 2011: Testing the Clausius–Clapeyron constraint on the aerosol-induced changes in mean and extreme precipitation. *Geophys. Res. Lett.*, **38**, L04807, doi:10.1029/2010GL046435.

Chou, C., and C. Lan, 2012: Changes in the annual range of precipitation under global warming. *J. Climate*, **25**, 222–235, doi:10.1175/JCLI-D-11-00097.1.

——, C.-A. Chen, P.-H. Tan, and K. T. Chen, 2012: Mechanisms for global warming impacts on precipitation frequency and intensity. *J. Climate*, **25**, 3291–3306, doi:10.1175/JCLI-D-11-00239.1.

Dai, A., 2006a: Recent climatology, variability and trends in global surface humidity. *J. Climate*, **19**, 3589–3606, doi:10.1175/JCLI3816.1.

——, 2006b: Precipitation characteristics in eighteen coupled climate models. *J. Climate*, **19**, 4605–4630, doi:10.1175/JCLI3884.1.

——, 2011: Drought under global warming: A review. *Wiley Interdiscip. Rev.: Climate Change*, **2**, 45–65, doi:10.1002/wcc.81.

——, 2013: Increasing drought under global warming in observations and models. *Nat. Climate Change*, **3**, 52–58, doi:10.1038/nclimate1633.

——, 2016: Historical and future changes in streamflow and continental runoff: A review. *Terrestrial Water Cycle and Climate Change: Natural and Human-Induced Impacts*, *Geophys. Monogr.*, Vol. 221, Amer. Geophys. Union, 17–37.

Durre, I., C. N. Williams Jr., X. Yin, and R. S. Vose, 2009: Radiosonde-based trends in precipitable water over the Northern Hemisphere: An update. *J. Geophys. Res.*, **114**, D05112, doi:10.1029/2008JD010989.

Ebita, A., and Coauthors, 2011: The Japanese 55-year reanalysis "JRA-55": An interim report. *SOLA*, **7**, 149–152, doi:10.2151/sola.2011-038.

Fu, C., and L. Dan, 2014: Trends in the different grades of precipitation over South China during 1960–2010 and the possible link with anthropogenic aerosols. *Adv. Atmos. Sci.*, **31**, 480–491, doi:10.1007/s00376-013-2102-7.

Goswami, B. N., V. Venugopal, D. Sengupta, M. S. Madhusoodanan, and P. K. Xavier, 2006: Increasing trend of extreme rain events over India in a warming environment. *Science*, **314**, 1442–1445, doi:10.1126/science.1132027.

Hasselmann, K., 1979: On the signal-to-noise problem in atmospheric response studies. *Meteorology over the Tropical Oceans*, B. D. Shaw, Ed., Royal Meteorological Society, 251–259.

——, 1993: Optimal fingerprints for the detection of time dependent climate change. *J. Climate*, **6**, 1957–1971, doi:10.1175/1520-0442(1993)006<1957:OFFTDO>2.0.CO;2.

Held, I. M., and B. J. Soden, 2006: Robust responses of the hydrological cycle to global warming. *J. Climate*, **19**, 5686–5699, doi:10.1175/JCLI3990.1.

IPCC, 2007: *Climate Change 2007: The Physical Science Basis*. S. Solomon et al., Eds., Cambridge University Press, 996 pp.

——, 2012: *Managing the Risks of Extreme Events and Disasters to Advance Climate Change Adaptation*. C. B. Field et al., Cambridge University Press, 582 pp.

——, 2013: *Climate Change 2013: The Physical Science Basis*. T. F. Stocker et al., Eds., Cambridge University Press, 1535 pp.

Jiang, Y., X. Liu, X. Q. Yang, and M. Wang, 2013: A numerical study of the effect of different aerosol types on East Asian summer clouds and precipitation. *Atmos. Environ.*, **70**, 51–63, doi:10.1016/j.atmosenv.2012.12.039.

Jiang, Z., Y. Shen, T. Ma, P. Zhai, and S. Fang, 2014: Changes of precipitation intensity spectra in different regions of mainland China during 1961–2006. *J. Meteor. Res.*, **28**, 1085–1098, doi:10.1007/s13351-014-3233-1.

Lamarque, J., and Coauthors, 2010: Historical (1850–2000) gridded anthropogenic and biomass burning emissions of reactive gases and aerosols: Methodology and application. *Atmos. Chem. Phys.*, **10**, 7017–7039, doi:10.5194/acp-10-7017-2010.

Lau, K.-M., and H.-T. Wu, 2007: Detecting trends in tropical rainfall characteristics, 1979–2003. *Int. J. Climatol.*, **27**, 979–988, doi:10.1002/joc.1454.

——, ——, and K.-M. Kim, 2013: A canonical response of precipitation characteristics to global warming from CMIP5 models. *Geophys. Res. Lett.*, **40**, 3163–3169, doi:10.1002/grl.50420.

Lee, S.-S., W.-K. Tao, and C.-H. Jung, 2014: Aerosol effects on instability, circulations, clouds, and precipitation. *Adv. Meteor.*, **2014**, 683950, doi:10.1155/2014/683950.

Liu, R., S. C. Liu, R. J. Cicerone, C.-J. Shiu, J. Li, J. L. Wang, and Y. H. Zhang, 2015: Trends of extreme precipitation in eastern China and their possible causes. *Adv. Atmos. Sci.*, **32**, 1027–1037, doi:10.1007/s00376-015-5002-1.

Liu, S. C., C. Wang, C. Shiu, H. Chang, C. Hsiao, and S. Liaw, 2002: Reduction in sunshine duration over Taiwan: Causes and implications. *Terr. Atmos. Ocean. Sci.*, **13**, 523–545.

——, C. Fu, C. J. Shiu, J. P. Chen, and F. Wu, 2009: Temperature dependence of global precipitation extremes. *Geophys. Res. Lett.*, **36**, L17702, doi:10.1029/2009GL040218.

Ma, S., T. Zhou, A. Dai, and Z. Han, 2015: Observed changes in the distributions of daily precipitation frequency and amount over China from 1960 to 2013. *J. Climate*, **28**, 6960–6978, doi:10.1175/JCLI-D-15-0011.1.

Menon, S., J. Hansen, L. Nazarenko, and Y. F. Luo, 2002: Climate effects of black carbon aerosols in China and India. *Science*, **297**, 2250–2253, doi:10.1126/science.1075159.

Min, S.-K., X. Zhang, and F. Zwiers, 2008: Human-induced Arctic moistening. *Science*, **320**, 518–520, doi:10.1126/science.1153468.

——, ——, F. W. Zwiers, and G. C. Hegerl, 2011: Human contribution to more-intense precipitation extremes. *Nature*, **470**, 378–381, doi:10.1038/nature09763.

Mitchell, J. F. B., T. C. Johns, J. M. Gregory, and S. F. B. Tett, 1995: Climate response to increasing levels of greenhouse gases and sulphate aerosols. *Nature*, **376**, 501–504, doi:10.1038/376501a0.

NCAR, 2012: NCAR command language, 6.0.0 ed. UCAR/NCAR/CISL/VETS, Boulder, CO, doi:10.5065/d6wd3xh5.

Pall, P., M. R. Allen, and D. A. Stone, 2007: Testing the Clausius–Clapeyron constraint on changes in extreme precipitation under CO_2 warming. *Climate Dyn.*, **28**, 351–363, doi:10.1007/s00382-006-0180-2.

——, T. Aina, D. A. Stone, P. A. Stott, T. Nozawa, A. G. Hilberts, D. Lohmann, and M. R. Allen, 2011: Anthropogenic greenhouse gas contribution to flood risk in England and Wales in autumn 2000. *Nature*, **470**, 382–385, doi:10.1038/nature09762.

Pendergrass, A. G., and D. L. Hartmann, 2014: The atmospheric energy constraint on global-mean precipitation change. *J. Climate*, **27**, 757–768, doi:10.1175/JCLI-D-13-00163.1.

Polson, D., G. C. Hegerl, R. P. Allan, and B. B. Sarojini, 2013: Have greenhouse gases intensified the contrast between wet and dry regions? *Geophys. Res. Lett.*, **40**, 4783–4787, doi:10.1002/grl.50923.

——, M. Bollasina, G. C. Hegerl, and L. J. Wilcox, 2014: Decreased monsoon precipitation in the Northern Hemisphere due to anthropogenic aerosols. *Geophys. Res. Lett.*, **41**, 6023–6029, doi:10.1002/2014GL060811.

Qian, W., J. Fu, and Z. Yan, 2007: Decrease of light rain events in summer associated with a warming environment in China during 1961–2005. *Geophys. Res. Lett.*, **34**, L11705, doi:10.1029/2007GL029631.

Qian, Y., D. Gong, J. Fan, L. R. Leung, R. Bennartz, D. Chen, and W. Wang, 2009: Heavy pollution suppresses light rain in China: Observations and modeling. *J. Geophys. Res.*, **114**, D00K02, doi:10.1029/2008JD011575.

Ramanathan, V., and Coauthors, 2005: Atmospheric brown clouds: Impact on South Asian climate and hydrologic cycle. *Proc. Natl. Acad. Sci. USA*, **102**, 5326–5333, doi:10.1073/pnas.0500656102.

Rosenfeld, D., U. Lohmann, G. B. Raga, C. D. O'Dowd, M. Kulmala, S. Fuzzi, A. Reissell, and M. O. Andreae, 2008: Flood or drought: How do aerosols affect precipitation? *Science*, **321**, 1309–1313, doi:10.1126/science.1160606.

Rotstayn, L., S. Jeffrey, M. Collier, S. Dravitzki, A. Hirst, J. Syktus, and K. Wong, 2012: Aerosol- and greenhouse gas-induced changes in summer rainfall and circulation in the Australasian region: A study using single-forcing climate simulations. *Atmos. Chem. Phys.*, **12**, 6377–6404, doi:10.5194/acp-12-6377-2012.

Seager, R., N. Naik, and G. Vecchi, 2010: Thermodynamic and dynamic mechanisms for large-scale changes in the hydrological cycle in response to global warming. *J. Climate*, **23**, 4651–4668, doi:10.1175/2010JCLI3655.1.

Shiu, C. J., S. C. Liu, C. Fu, A. Dai, and Y. Sun, 2012: How much do precipitation extremes change in a warming climate? *Geophys. Res. Lett.*, **39**, L17707, doi:10.1029/2012GL052762.

Song, F., T. Zhou, and Y. Qian, 2014: Responses of East Asian summer monsoon to natural and anthropogenic forcings in the 17 latest CMIP5 models. *Geophys. Res. Lett.*, **41**, 596–603, doi:10.1002/2013GL058705.

Sun, F., M. L. Roderick, and G. D. Farquhar, 2012: Changes in the variability of global land precipitation. *Geophys. Res. Lett.*, **39**, L19402, doi:10.1029/2012GL053369.

Sun, Y., S. Solomon, A. Dai, and R. W. Portmann, 2007: How often will it rain? *J. Climate*, **20**, 4801–4818, doi:10.1175/JCLI4263.1.

Taylor, K. E., R. J. Stouffer, and G. A. Meehl, 2012: An overview of CMIP5 and the experiment design. *Bull. Amer. Meteor. Soc.*, **93**, 485–498, doi:10.1175/BAMS-D-11-00094.1.

Trenberth, K. E., A. Dai, R. M. Rasmussen, and D. B. Parsons, 2003: The changing character of precipitation. *Bull. Amer. Meteor. Soc.*, **84**, 1205–1218, doi:10.1175/BAMS-84-9-1205.

——, J. Fasullo, and L. Smith, 2005: Trends and variability in column-integrated atmospheric water vapor. *Climate Dyn.*, **24**, 741–758, doi:10.1007/s00382-005-0017-4.

——, L. Smith, T. Qian, A. Dai, and J. Fasullo, 2007: Estimates of the global water budget and its annual cycle using observational and model data. *J. Hydrometeor.*, **8**, 758–769, doi:10.1175/JHM600.1.

Westra, S., L. V. Alexander, and F. W. Zwiers, 2013: Global increasing trends in annual maximum daily precipitation. *J. Climate*, **26**, 3904–3918, doi:10.1175/JCLI-D-12-00502.1.

Wild, M., J. Grieser, and C. Schar, 2008: Combined surface solar brightening and increasing greenhouse effect support recent intensification of the global land-based hydrological cycle. *Geophys. Res. Lett.*, **35**, L17706, doi:10.1029/2008GL034842.

Willett, K. M., P. D. Jones, P. W. Thorne, and N. P. Gillett, 2010: A comparison of large scale changes in surface humidity over land in observations and CMIP3 general circulation models. *Environ. Res. Lett.*, **5**, 025210, doi:10.1088/1748-9326/5/2/025210.

Wu, L., H. Su, and J. H. Jiang, 2013: Regional simulation of aerosol impacts on precipitation during the East Asian summer monsoon. *J. Geophys. Res. Atmos.*, **118**, 6454–6467, doi:10.1002/jgrd.50527.

Wu, P., N. Christidis, and P. Stott, 2013: Anthropogenic impact on Earth's hydrological cycle. *Nat. Climate Change*, **3**, 807–810, doi:10.1038/nclimate1932.

Ye, J., W. Li, L. Li, and F. Zhang, 2013: "North drying and south wetting" summer precipitation trend over China and its potential linkage with aerosol loading. *Atmos. Res.*, **125–126**, 12–19, doi:10.1016/j.atmosres.2013.01.007.

Zhang, Q., K. B. He, and H. Huo, 2012: Cleaning China's air. *Nature*, **484**, 161–162, doi:10.1038/484161a.

Zhang, X., F. W. Zwiers, G. C. Hegerl, F. H. Lambert, N. P. Gillett, S. Solomon, P. A. Stott, and T. Nozawa, 2007: Detection of human influence on twentieth-century precipitation trends. *Nature*, **448**, 461–465, doi:10.1038/nature06025.

——, H. Wan, F. W. Zwiers, G. C. Hegerl, and S.-K. Min, 2013: Attributing intensification of precipitation extremes to human influence. *Geophys. Res. Lett.*, **40**, 5252–5257, doi:10.1002/grl.51010.

Zhao, T., and A. Dai, 2015: The magnitude and causes of global drought changes in the 21st century under a low–moderate emissions scenario. *J. Climate*, **28**, 4490–4512, doi:10.1175/JCLI-D-14-00363.1.

——, ——, and J. Wang, 2012: Trends in tropospheric humidity from 1970 to 2008 over China from a homogenized radiosonde dataset. *J. Climate*, **25**, 4549–4567, doi:10.1175/JCLI-D-11-00557.1.

Zhou, T.-J., and R.-C. Yu, 2005: Atmospheric water vapor transport associated with typical anomalous summer rainfall patterns in China. *J. Geophys. Res.*, **110**, D08104, doi:10.1029/2004JD005413.